Journal of Advanced Ceramics
先进陶瓷
ISSN 2226-4108
CN 10-1154/TQ
清華大学出版社 Tsinghua University Press
SciOpen

J Adv Ceram 2026, **15**: 9221374

https://doi.org/10.26599/JAC.2026.9221374

Research Article

Cold-Sintered phosphor film@Cu converter for ultra-high-brightness laser illumination

Jiuzhou Zhao[1], Meiqi Ye[1], Wenhao Zhang[1], Guankai Wang[1], Yun Mou[2], Yang Peng[1,*]

[1] *Huazhong University of Science and Technology, School of Aerospace Engineering, Wuhan 430074, China.*

[2] *Shenzhen Campus of Sun Yat-Sen University, School of Integrated Circuits, Shenzhen 518107, China*

* Corresponding author.

E-mail: ypeng@hust.edu.cn

Received: July 7, 2026; Revised: August 17, 2026; Accepted: September 4, 2026

清華大学出版社 Tsinghua University Press | SciOpen

Abstract: Phosphor ceramic has been regarded as a promising color converter for high-quality laser illumination, but it often suffers from optothermal performance degradation during high-temperature sintering process. Herein, an optothermal-enhanced cold-sintered phosphor film@Cu (PF@Cu) converter is developed. A low-temperature (150°C) cold sintering process (CSP) was introduced and tunable composite pastes were prepared with geopolymer, alkali activator, and phosphor materials. High-performance yellow-emitting PF@Cu (Y-PF@Cu) and yellow/red-emitting PF@Cu (Y/R-PF@Cu) converters were prepared with densified PFs that tightly integrated with the Cu substrate while effectively preserving the intrinsic luminescent properties of phosphors. The optimized Y-PF@Cu converter achieves a record luminous flux (LF) of 9624.7 lm@35 W/mm^2, a correlated color temperature (CCT) of 5931 K and a color rendering index (CRI) of 60.7. The further optimized Y/R-PF@Cu converter delivers excellent comprehensive performance, including a high thermal conductivity of 50.6 W/(m·K), a LF of 2652.2 lm@17.5 W/mm^2, a CCT of 2604 K, and a significantly improved CRI of 91.2. This work demonstrates the feasibility of CSP for fabricating color converters and provides an efficient strategy for synergistic optothermal optimization in ultra-high-brightness laser-illumination applications.

Keywords: laser lighting; cold sintering; phosphor film; optothermal robust; inorganic phosphor converter

1 Introduction

Laser lighting is emerging as a next-generation high-brightness semiconductor light source, with broad applications spanning automotive lighting, advanced display and projection systems, and high-speed optical information transmission [1-3]. Laser-excited phosphor (LEP) technology is widely adopted for achieving high-brightness white laser light sources, in which the most straightforward and commonly used configuration relies on blue laser diode (LD) excitation of yellow phosphor converters

[4-6]. Driven by increasing application demands, excitation laser power has steadily increased, prompting the replacement of traditional phosphor-in-resin converters by inorganic phosphor converters [7,8]. Typical representatives include single crystals (SCs) [9], phosphor-in-glass (PiG) [10], phosphor-in-glass film (PiGF) [11-13], and phosphor ceramic (PC) [14,15]. Unfortunately, the SCs still suffer from limitations in thermal management and large-scale fabrication [16]. Both PiG and PiGF employ glass as the host matrix, which has inherently low thermal conductivity, leading to pronounced local heat accumulation and luminescence saturation under high-power laser excitation, thereby limiting their long-term stability [17,18].

Conventional PC converters present outstanding advantages in thermal conductivity, which are fabricated by uniformly mixing phosphor powders within ceramic powders, followed by densification through high-temperature (>1500℃) sintering. The ceramic matrix not only acts as light-scattering centers to enhance light extraction efficiency and light uniformity, but also provides intrinsically high thermal conductivity, facilitating rapid heat transfer and dissipation around phosphors [19,20]. Consequently, the PC converters combine high heat-dissipation efficiency and tunable synergistic optothermal properties, making them a promising option for advanced luminescent conversion materials [21]. For high-brightness white laser illumination, $Y_3Al_5O_{12}:Ce^{3+}$ (YAG) yellow-emitting phosphor is widely adopted due to its high quantum efficiency and well-established lighting system [22,23]. Xie et al. [24] mixed the YAG phosphor with Al_2O_3 powders to prepare an Al_2O_3-YAG PC converter, presenting enhanced overall thermal conductivity (~30 W/m·K) and an elevated laser power density saturation threshold (LPD-ST) of 22 W/mm^2. Since the emission of Ce^{3+} in the YAG lattice is mainly centered at ~550 nm, the red emission component is insufficient, leading to a low color rendering index (CRI) and a high correlated color temperature (CCT), thus limiting the application in high-quality white laser lighting [25].

To address this limitation, the red-emitting phosphor (typically $CaAlSiN_3:Eu^{2+}$ (CASN)) has been developed and extensively studied [26,27]. By co-introducing CASN with YAG into a ceramic matrix, hybrid PC converters that realize synergistic yellow-red emission under blue laser excitation have been constructed, thereby forming a broad-spectrum laser lighting system [28]. Studies by Jiang et al. [29] and Chen et al. [30] demonstrated that as the red-emitting phosphor content increases, the CRI of white laser light is progressively improved, while the CCT is correspondingly reduced. Nevertheless, the fabrication of PC converters typically relies on high-temperature (>1500℃) densification processes such as vacuum sintering [31], hot pressing [32], and spark plasma sintering [33], often requiring prolonged holding times (>5 h) to achieve structural consolidation. These harsh conditions adversely affect the optical performance of PC converters. On one hand, the elevated sintering temperature induces thermal quenching of both YAG and CASN phosphors. The CASN phosphor is particularly susceptible to high-temperature degradation, exhibiting more pronounced thermal decomposition and nitrogen volatilization, leading to severe optical performance degradation [34,35]. On the other hand, high-temperature sintering may trigger interfacial chemical reactions and elemental interdiffusion between YAG and CASN, forming non-radiative recombination layers that further reduce the overall luminous efficacy (LE) [36]. Moreover, during operation, the PC converter is subjected to high-power-density blue laser excitation, which generates localized high temperatures at the laser spot, exacerbating the thermal quenching of phosphor and reducing overall LE [37,38]. Therefore, developing a low-temperature fabrication alternative strategy for the phosphor converter is of vital importance for improving the photothermal characteristics. Recently, Wang et al. [39] proposed a second-level fast sintering as an alternative strategy to reduce the adverse effects of prolonged high-temperature processing, enabling $Lu_3Al_5O_{12}$–$CaAlSiN_3$ composite ceramics to be rapidly densified at 1650℃ within only 1-30 s. Although this strategy substantially shortens the thermal exposure time, the phosphors are still subjected to extremely high temperatures, motivating the development of a fundamentally low-temperature consolidation route.

The cold sintering process (CSP) offers a promising strategy for constructing novel color converters. By using low temperatures (<350℃) and high pressures (hundreds of MPa) for uniformly mixed composite paste including thermal conductive matrix material and luminescent material, the CSP facilitates matrix densification and ensures close interfacial contact between the matrix and thermally sensitive phosphor particles, thereby forming efficient thermal conduction pathways [40]. The lattice stability of luminescent centers, such as Ce^{3+} in YAG and Eu^{2+} in CASN, is maintained. The interfacial elemental interdiffusion and chemical reactions between CASN and YAG are suppressed. Moreover, by tuning the CSP parameters including liquid-phase composition, pressure, and holding time, precise control over the matrix material microstructure can be achieved [41,42]. Consequently, fabricating optothermal-enhanced phosphor film (PF) converters based on CSP is technically feasible.

Herein, cold-sintered phosphor film@Cu (PF@Cu) converter for ultra-high-brightness laser illumination were proposed. YAG yellow-emitting phosphor (Y-Phosphor), CASN red-emitting phosphor (R-Phosphor), and their composite (Y/R-Phosphor) were selected as the luminescent materials, while geopolymer incorporating a trace amount of alkali activator served as the matrix material. The materials were uniformly mixed to form a series of composite paste. Using CSP at 150°C and 150 MPa, yellow-emitting PF@Cu (Y-PF@Cu), red-emitting PF@Cu (R-PF@Cu), and yellow/red-emitting PF (Y/R-PF@Cu) converters were fabricated on Cu substrate. The material properties and optothermal performances of PF@Cu converters were systematically investigated. The optimal component for Y-PF@Cu and Y/R-PF@Cu converters were determined. The beneficial effects of Y/R-PF@Cu converter over its Y-PF@Cu counterpart were comparatively evaluated. The application prospects of Y-PF@Cu converter in high-brightness laser illumination were confirmed.

2 Experimental

2. 1 Fabrication of cold-sintered PF@Cu converters

Y-PF@Cu, R-PF@Cu, and Y/R-PF@Cu converters were fabricated via CSP, as illustrated in Fig. 1(a-c). First, three types of composite pastes were prepared. The matrix material of all composite pastes is consisted of geopolymer (metakaolin, Sinopharm, China) and alkali activator (sodium aluminosilicate, Sinopharm, China). For the first paste, intended for Y-PF@Cu converters, the luminescent material was only Y-Phosphor (YAG, Intematix, USA), with geopolymer-Y-Phosphor (G-Y) mass ratios of 1-1, 1-2, 1-3, 1-4, and 1-5. For the second paste, developed for R-PF@Cu converters, the luminescent material was only R-Phosphor (CASN, Intematix, USA) with fixed geopolymer-R-Phosphor (G-R) mass ratio of 1-0.5. For the third paste, prepared for optimized Y/R-PF@Cu converters, the luminescent materials included both Y-Phosphor and R-Phosphor, with a G-Y mass ratio fixed at 1-4 and an adjustable R-Phosphor content to obtain G-Y-R mass ratios of 1-4-0.1, 1-4-0.2, 1-4-0.3, 1-4-0.4, and 1-4-0.5. Thereafter, the materials were weighed separately and then mixed in a mortar. The mixture was thoroughly ground until a homogeneous paste with slight viscosity formed, which was set aside for later use.

The material assembly form for CSP is depicted in Fig. 1(b). The central cavity of holder was cylindrical, with a base at the bottom. On top of the base, a support block (stainless steel, diameter 30 mm, thickness 5 mm) was first placed to provide a flat supporting surface, followed by a Cu substrate (diameter 30 mm, thickness 5 mm) serving as the heat sink for the PF@Cu converters, then the composite paste, and finally another support block. After assembly, the holder was subjected to CSP, and the equipment is illustrated in Fig. 1(c). During this process, a temperature of 150℃ and a vertical pressure of 150 MPa were simultaneously applied and maintained for 3 h. A series of Y-PF@Cu, R-PF@Cu, and Y/R-PF@Cu converters with different optothermal characteristics was successfully fabricated.

2. 2 Characterization

Photographs of Y-PF@Cu and Y/R-PF@Cu converters under daylight and UV light were captured using a digital camera (XS-10, Fujifilm, Japan). The micromorphology of the three categories of PF@Cu converters was characterized by field-emission scanning electron microscopy (FE-SEM, RISE-CLARA, TESCAN WITec, Czech Republic and Germany), with critical elemental distribution determined by energy-dispersive X-ray spectroscopy (EDS) attached. In terms of material performance characterization, the material features of Y-PF@Cu, R-PF@Cu, and Y/R-PF@Cu converters were examined, and the pristine Y-Phosphor and R-Phosphor were included as references. The photoluminescence excitation (PLE), photoluminescence (PL) spectra, and fluorescence decay curves were examined by a fluorescence spectrometer (QuantaMaster 8500, Horiba Instruments, Canada). The temperature-dependent PL spectra and internal quantum efficiency (IQE) were measured by the Edinburgh fluorescence spectrometer (FLS1000, UK). The phase composition was determined by X-ray diffraction (XRD, Smart Lab 9KW, Rigaku Corporation, Japan) over a 2θ range of 10°-80°.

The optical characteristics of Y-PF@Cu, R-PF@Cu, and Y/R-PF@Cu converters, including luminous flux (LF), LE, LPD-ST, CCT, CRI, CIE chromaticity coordinates, and electroluminescence (EL) spectra, were examined. The test system was self-developed and consisted mainly of a high-power blue laser source (450 nm, light spot 2 mm^2, adjustable power range 3~200 W, RAYCUS, China), a spectroradiometer (HAAS-2000, EVERFINE, China), and an integrating sphere (diameter 50 cm). Inside the integrating sphere, a supporting stage was positioned at the center to fix the test sample, ensuring concentric alignment between the sample center and the laser beam. By comparing optical performance comprehensively, the Y/R-PF@Cu converters with the best overall optical characteristics were selected for thermal evaluation. The thermal conductivity coefficient was measured by thermal constant analyzer (TPS2500S, Hot Disk, Sweden). The thermostability under long-term high-power laser irradiation at 5~15 W/mm^2 (0~270 s) was monitored using an infrared thermal imager (E63, FLIR, USA).

3 Results and discussion

Fig. 1(d) presents the photographs of Y-PF@Cu and Y/R-PF converters under daylight and UV light. Under daylight, the Y-PF@Cu and Y/R-PF@Cu converters exhibit distinct color variations. As the Y-Phosphor content increases, the Y-PF@Cu converters transition from dark yellow to bright yellow; with rising R-Phosphor content, the Y/R-PF@Cu converters change from light orange to deep orange. Under UV light, both types of converters exhibit uniform fluorescent emission, with intensity increasing proportionally to phosphor content. The Y-PF@Cu converters shift from dark yellow to bright yellow with increasing Y-Phosphor content, while the Y/R-PF@Cu converters evolve from bright orange to bright red with higher R-Phosphor content. The Y-PF@Cu and Y/R-PF@Cu converters exhibit uniform macroscopic appearances under daylight and relatively uniform fluorescence emission under UV irradiation, indicating successful fabrication of the PF@Cu converters by CSP.

Fig. 1(e-m) presents the surface and cross-sectional microstructure and elemental distribution of Y/R-PF@Cu converter. As shown in Fig. 1(e), the phosphor powders are uniformly distributed within the matrix with no observable interfacial defects or cracks, confirming that the CSP process ensures the structural integrity of Y/R-PF@Cu converter. In the EDS elemental mapping images (Fig. 1(f-i)), Y, Ca, and Al are detected. Y is the characteristic element of Y-Phosphor and is extensively distributed across the entire surface due to its high content. Ca, the characteristic element of R-Phosphor, is present in smaller amounts and maintains a slightly sparse and uniform distribution. Al exists in the geopolymer, alkali activator, Y-Phosphor, and R-Phosphor, distributing across the entire surface with localized aggregation. For the cross-section shown in Fig. 1(j), the PF remains tightly bonded to the Cu substrate without noticeable gaps. The intimate PF/Cu interface can be mainly attributed to the pressure-assisted consolidation during CSP. Under a pressure of 150 MPa, the wet composite paste is compacted against the Cu surface, which promotes conformal contact, reduces interfacial voids, and increases the effective contact area. Meanwhile, the liquid phase introduced by the alkali activator facilitates particle rearrangement and geopolymer consolidation at 150°C, helping to retain the compact interface after solidification and thereby reducing the interfacial thermal resistance. The elemental distribution characteristics of cross-section are illustrated in Fig. 1(k-m). The upper region corresponds to the PF, where Si and Y are enriched. Si is distributed across the entire cross-section and originates mainly from the geopolymer, R-Phosphor, and alkali activator. Y, as the characteristic element of Y-Phosphor, is uniformly distributed within the matrix. These results demonstrate that after CSP, the geopolymer and alkali activator form the complete skeleton of matrix, effectively supporting the PF structure. Both Y-Phosphor and R-Phosphor are distributed uniformly in the matrix and maintain good structural integrity with no interfacial reaction. The intimate contact between phosphor powders and surrounding matrix ensures excellent heat dissipation, providing crucial structural support for optothermal enhancement.

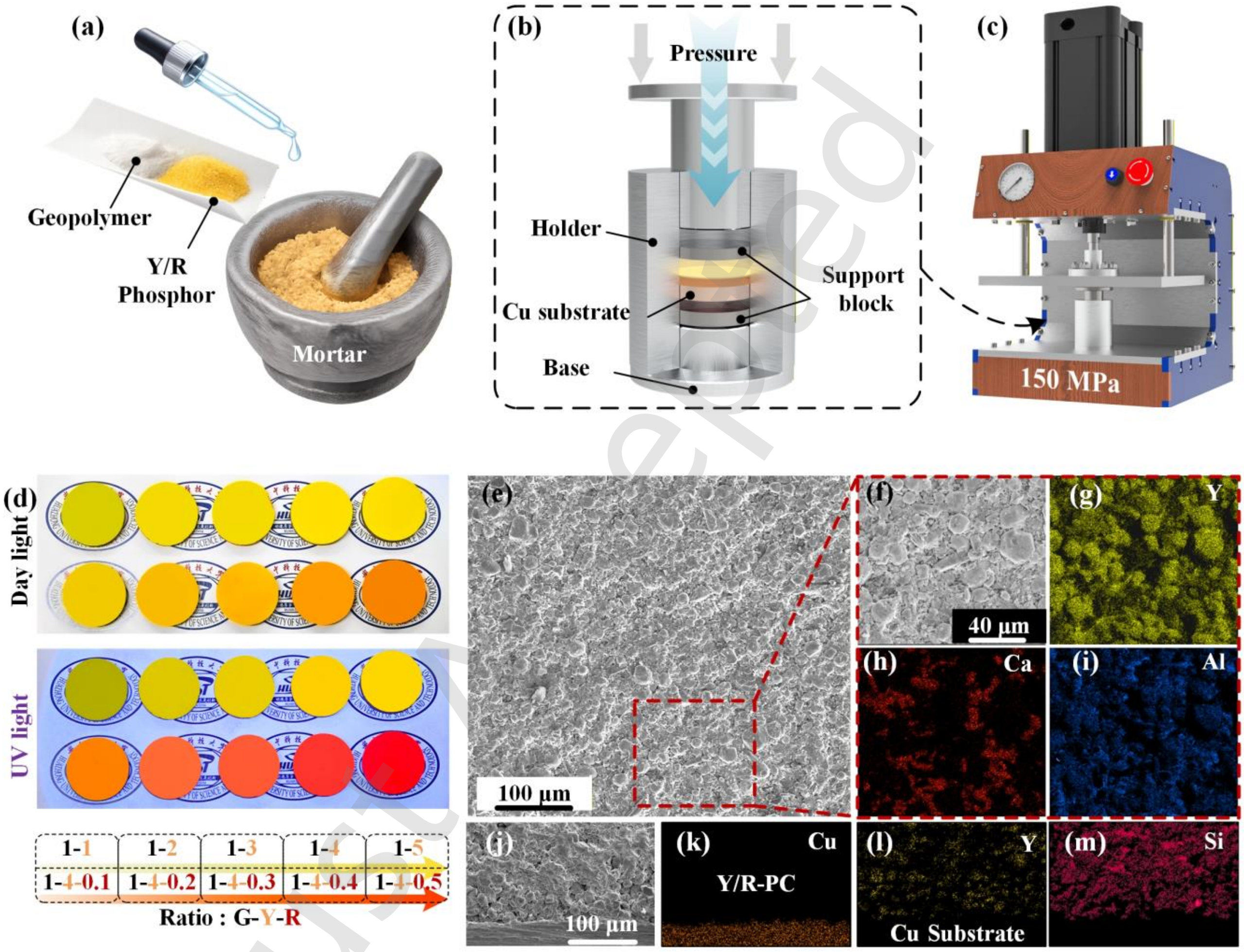

Fig.1 CSP of PF@Cu converters. (a) Preparation of composite paste. (b) Material assembly form and (c) equipment. (d) Fabricated Y-PF@Cu and Y/R-PF@Cu converters. Micromorphology and EDS elemental mapping images of Y/R-PF@Cu converter (e-i) surface and (j-m) cross-section.

As presented in Fig. 2(a), the Y-PF@Cu converter with G-Y mass ratios of 1-4 has an excitation peak centered at approximately 468 nm originating from the Ce^{3+}: 5d→4f electron transition in PLE spectra, and displays broadband emission centered at approximately 535 nm under 450 nm light excitation in PL spectra. The R-PF@Cu with G-R mass ratios of 1-0.5 converter exhibits broadband emission from 300 nm to 600 nm in PLE spectra, deriving from 5d→4f electron transitions of Eu^{2+}, while displaying broadband emission at about 657 nm in PL spectra under 450 nm light excitation. Notably, the PLE and PL spectra of both the Y-PF@Cu converter and the R-PF@Cu converter are similar to those of raw phosphors, indicating that the prepared PF@Cu converters maintain the luminescent properties of Y-Phosphor and R-Phosphor under CSP. For the Y/R-PF@Cu converter with G-Y-R mass ratios of 1-4-0.5, the PLE spectra integrate the excitation features of both Y-Phosphor and R-Phosphor, exhibiting a broad excitation band spanning approximately 430~500 nm, with a dominant peak centered at 535 nm. Under 450 nm light excitation, the PL spectra display a broad emission band coverage across the yellow-to-red region with a peak centered at about 655 nm. No obvious shift or degradation of the raw Y-Phosphor and R-Phosphor is observed.

The IQE values are shown in Fig. 2(b). The Y-PF@Cu and R-PF@Cu converters exhibited only slight attenuation relative to the raw phosphors, with IQE decreasing from 95.4% to 92.5% and from 88.1% to 86.6%, respectively. Notably, the Y/R-PF@Cu converter achieves a high IQE of 90.1%. According to the phase composition in Fig. 2(c), the diffraction peaks of Y-Phosphor and Y-PF@Cu converter, as well as those of R-Phosphor and R-PF@Cu converter, are highly consistent, with only minor differences in peak intensity, indicating that both Y-Phosphor and R-Phosphor maintain an intact crystal within the matrix of PF@Cu converters. As presented in Fig. 2(d), the fluorescence lifetimes of Y-Phosphor, Y-PF@Cu converter, R-Phosphor, R-PF@Cu converter, and Y/R-PF@Cu converter are 67.43, 62.81, 719.12, 718.73, and 761.43 ns, respectively, resulting in negligible lifetime differences between PF@Cu converters and the corresponding raw phosphor. Particularly, the Y/R-PF@Cu converter exhibits the longest fluorescence lifetime, which is dominated by the longer-lived R-Phosphor component, and additional radiative reabsorption/reemission between the two phosphor phases may further prolong the effective lifetime. In the temperature-dependent PL spectra (Fig. 2 (e)), the spectra intensity of Y-Phosphor, Y-PF@Cu converter, R-Phosphor, R-PF@Cu converter, and Y/R-PF@Cu converter decreases with temperature from 20℃ to 230℃, with Y-Phosphor and R-Phosphor showing a higher decline rate than their PF@Cu counterparts. Collectively, these beneficial effects are attributed to the intrinsic phosphor properties preservation and matrix densification by CSP, which enables efficient heat dissipation around the phosphor particles, thereby ensuring stable luminescence in the PF@Cu converters.

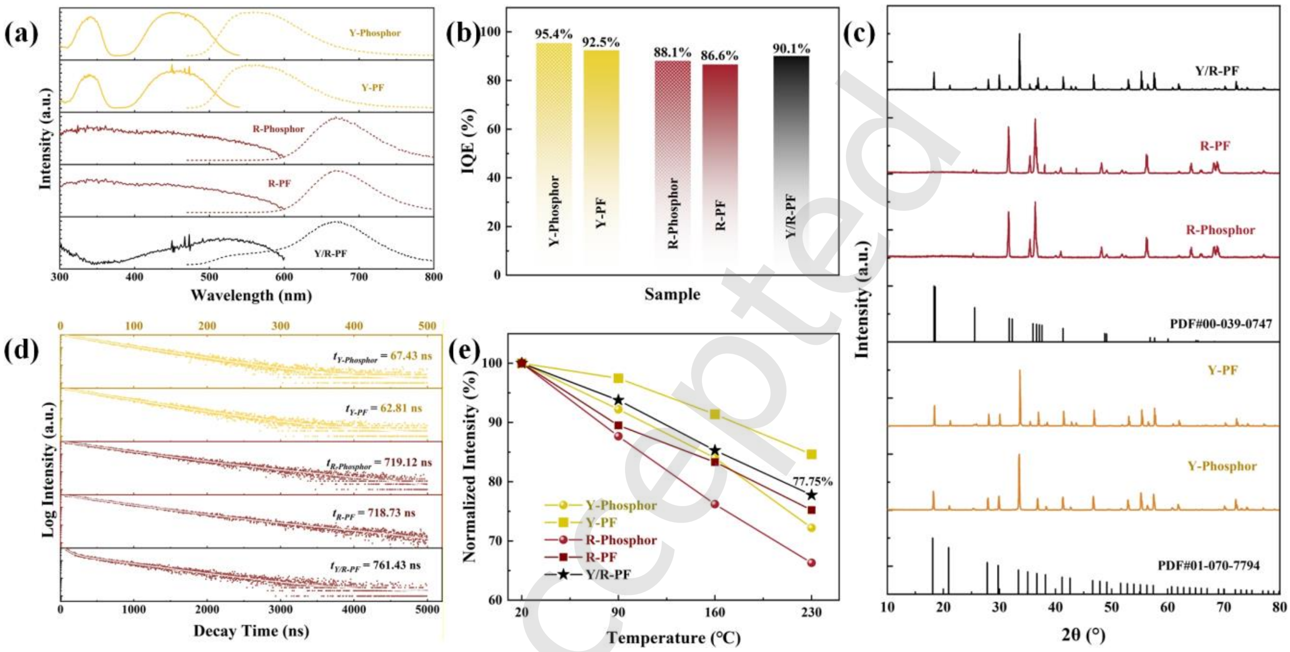

Fig. 2 Material characteristics of PF@Cu converters. (a) PLE and PL spectra, (b) IQE, (c) phase composition, (d) fluorescence decay curves, and (e) temperature-dependent PL spectra.

The optical performances of Y-PF@Cu converters with different G-Y mass ratios under varying LPD are summarized in Fig. 3. As shown in Fig. 3(a), the LF initially increases with LPD until reaching LPD-ST. In Fig. 3(b), the LE gradually decreases with LPD until LPD-ST, and continuously increases with higher phosphor content. The LPD-ST and the corresponding max LF in Fig. 3(c) both first increase and then decrease with G-Y mass ratio, reaching their optimal values at a G-Y mass ratio of 1-4, corresponding to an LPD-ST of 35 W/mm^2 and a maximum LF of 9624.7 lm. As shown in Fig. 3(d), the CCT remains stable below the LPD-ST but increases sharply once it is exceeded. In Fig. 3(e), the CRI shows minor fluctuations with LPD, remaining in the range of 60~62, indicating generally limited color quality. The CIE chromaticity coordinates in Fig. 3(f) shift along the Planck curve with increasing G-Y mass ratio, accompanied by a decrease in CCT from 23351 K to 5443 K. These behaviors are attributed to the trade-off between enhanced light extraction at higher phosphor loading and deteriorated heat dissipation due to reduced matrix content. Consequently, a G-Y mass ratio of 1-4 achieves the best optothermal balance.

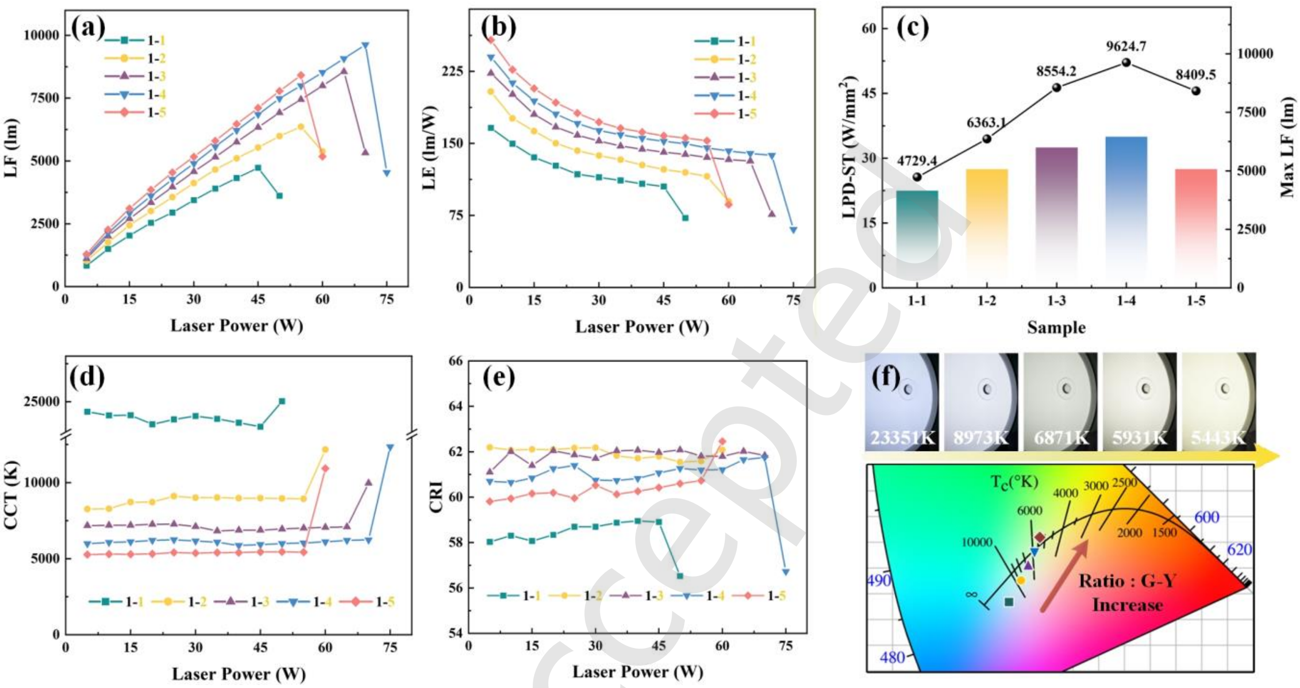

Fig. 3 Optical performance of Y-PF@Cu converters with different G-Y mass ratios. (a) LF, (b) LE, (c) LPD-ST and corresponding max LF, (d) CCT, (e) CRI, and (f) CIE chromaticity coordinates at LPD of 35 W/mm^2.

Since the CCT and CRI of the optimal Y-PF@Cu converters still have room for improvement, R-Phosphor was introduced with adjustable content to form Y/R-PF@Cu converters. The optical performances of Y/R-PF@Cu converters with different G-Y-R mass ratios under varying LPD are summarized in Fig. 4. As shown in Fig. 4(a), the LF initially increases with LPD until reaching LPD-ST, while decreasing with R-Phosphor content. In Fig. 4(b), the LE not only gradually decreases with LPD until LPD-ST, but also decreases with R-Phosphor content. The LPD-ST and corresponding max LF in Fig. 4(c) both decrease from 9624.7 lm to 2652.2 lm with the G-Y-R mass ratio, which still maintained a relatively high value. As shown in Fig. 4(d), the CCT decreases with R-Phosphor content, and remains stable below LPD-ST but increases sharply once the threshold is exceeded. In Fig. 4(e), the yellow emission intensity decreases continuously, while the red emission intensity gradually increases with the G-Y-R mass ratio, centered at 535 nm and 653 nm, respectively. The CIE chromaticity coordinates in Fig. 4(f) shift across the Planck curve with increasing G-Y-R mass ratio, accompanied by a decrease in CCT from 4741 K to 2604 K, indicating a transition toward warm white light. In Fig. 4(f), the CRI initially increases rapidly with the G-Y-R mass ratio and then gradually stabilizes, reaching a maximum value of 91.2. Overall, the optimal Y/R-PF@Cu converter is obtained at a G-Y-R mass ratio of 1-4-0.5. In Fig. 4(h), billiards with various colors are illuminated by the optimized Y-PF@Cu converter-based (G-Y = 1-4), Y/R-PF@Cu converter-based (G-Y-R = 1-4-0.5) white LD sources, and under daylight, respectively. The Y/R-PF@Cu converter enables high-quality white LD emission, rendering objects with more vivid, natural colors that closely match those observed under daylight illumination.

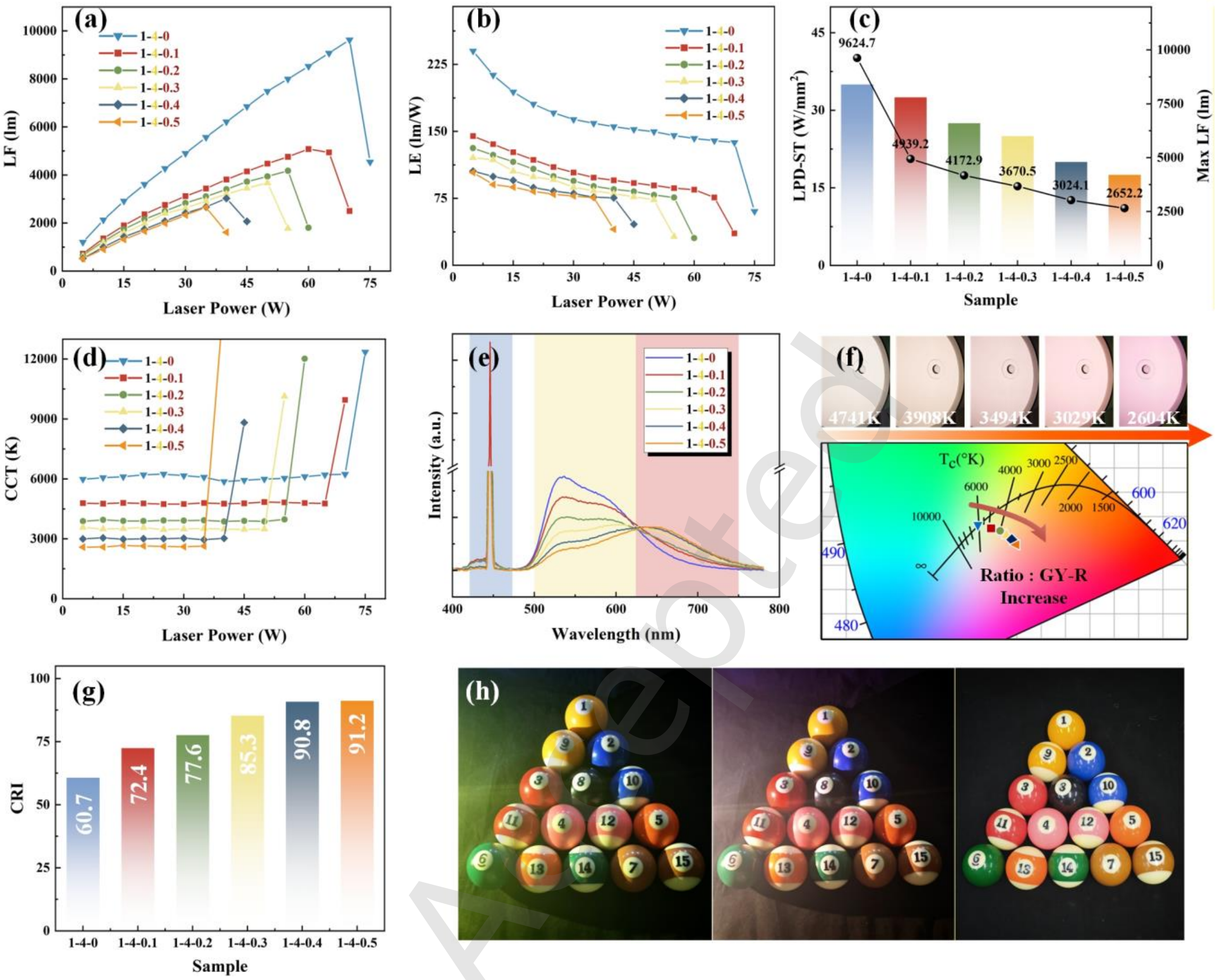

Fig. 4 Optical performance of Y/R-PF@Cu converters with different G-Y-R mass ratios. (a) LF, (b) LE, (c) LPD-ST and corresponding max LF, (d) CCT, (e) EL spectra, (f) CIE chromaticity coordinates, and (g) CRI at LPD of 17.5 W/mm^2. (h) Demonstration experiment of illuminating billiards under the Y-PF@Cu converter-based (G-Y = 1-4), Y/R-PF@Cu converter-based (G-Y-R = 1-4-0.5) white LD sources, and daylight.

The optothermal enhancement mechanism of Y/R-PF@Cu converter can be explained by the schematic shown in Fig. 5(a). In the reflective configuration, the geopolymer serves as a high-thermal-conductivity matrix, tightly encapsulating the embedded Y-Phosphor and R-Phosphor to form efficient heat-transfer pathways. Meanwhile, the Cu substrate is intimately bonded to the PF and acts as an effective heat sink, facilitating rapid heat dissipation. These synergistic effects significantly enhance the thermal management of both phosphors and effectively suppress thermal quenching under high-power blue laser excitation. Table 1 broadly compares the optical performance of representative reflective converters driven by blue LD. Despite differences in materials, fabrication methods, and testing conditions, the results highlight the potential advantages of CSP-based PF@Cu converters in low-temperature fabrication and overall optical performance.

Table 1 Reported optical performance of reflective color converters.

Color converter	Preparation temperature (°C)	Optical performance				Ref.
		LF (lm)	CRI	CCT (K)	LPD-ST (W/mm^2)	
$PiGF@Al_2O_3$	640	4510	80.0	3541	16.9	[6]
YAG:Ce PC	1780	1250	59.5	4478	20.3	[19]
$Lu_3Al_5O_{12}:Ce^{3+}/(Sr,Ca)AlSiN_3:Eu^{2+}$	1760	428.5	95.6	3344	28.76	[20]
$Y_3Al_5O_{12}:Ce^{3+}/Al_2O_3$	1700	1554	61.4	3769.7	48.5	[37]
YAG–YAG:Ce	1350	1060	66	5298	6.68	[32]
Y-PF@Cu	150	9624.7	62	5443	35	This work
Y/R-PF@Cu	150	2652.2	91.2	2604	17.5	

The overall thermal conductivity of Y/R-PF@Cu converter is measured to be 50.6 W/(m·K). The corresponding thermal behavior is presented in Fig. 5(b-c). Under continuous laser irradiation for 5 min, the Y/R-PF@Cu converter exhibits excellent heat dissipation capability and thermal stability. As the LPD increases from 5 to 15 W/mm^2, the surface temperature of Y/R-PF@Cu converter rises rapidly at the initial stage and then reaches a steady state with prolonged irradiation. The highest temperature is observed at the laser spot, while the surrounding regions also gradually increase with time, indicating efficient intrinsic heat conduction. At a power density of 15 W/mm^2, the maximum temperature is only 327°C, further confirming the superior thermal performance of the Y/R-PF@Cu converter. The compact PF/Cu interface and rapid heat spreading of the Cu substrate help reduce thermal stress, thereby suppressing delamination and cracking of the overall structure.

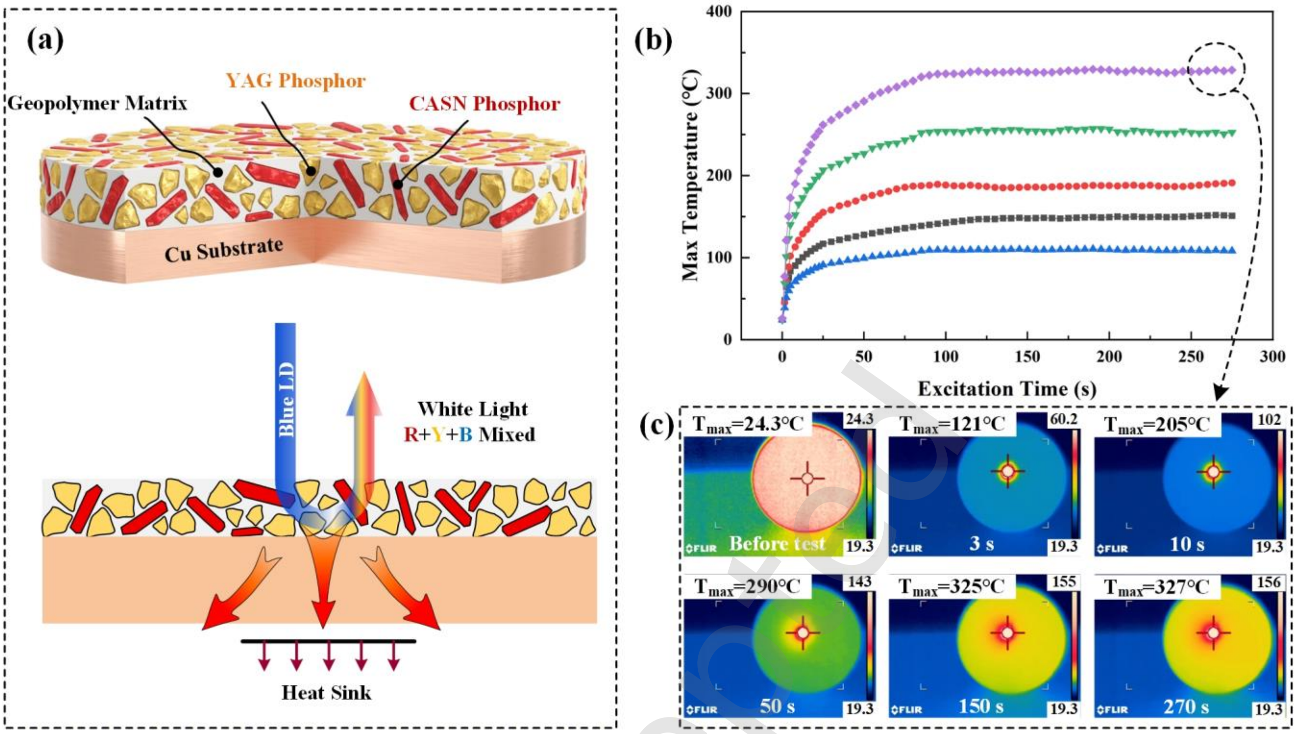

Fig. 5 Thermal performance of optimized Y/R-PF@Cu converter. (a) Schematic of optical-heat transfer in the Y/R-PF@Cu converter. (b) Max temperature under various LPD and irradiation times. (c) Temperature distribution of Y/R-PF@Cu converter under various irradiation times with LPD of 15 W/mm^2.

4 Conclusions

In this work, we developed optothermal-enhanced cold-sintered PF@Cu converters for ultra-high-brightness laser illumination. The Y-PF@Cu and Y/R-PF@Cu converters were fabricated on Cu substrates using a series of composite pastes containing geopolymer, alkali activator, and fluorescent material via CSP at 150℃ and 150 MPa. The optothermal performance of Y-PF@Cu converter and Y/R-PF@Cu converter was continuously optimized by adjusting the mass ratios of G-Y and G-Y-R. The effect of low-damage CSP on the optothermal performance of Y-PF@Cu and Y/R-PF@Cu converters was investigated at various LPDs. The optimal component ratios for Y-PF@Cu and Y/R-PF@Cu converters were determined. Compared with the Y-PF@Cu counterpart, the Y/R-PF@Cu converter exhibits significantly enhanced overall performance. The optimized Y-PF@Cu converter with a G-Y mass ratio of 1-4 achieves an LPD-ST of 35 W/mm^2, a max LF of 9624.7 lm, a CCT of 5931 K, and a CRI of 60.7. In contrast, the further-optimized Y/R-PF@Cu converter with a G-Y-R mass ratio of 1-4-0.5 delivers an LPD-ST of 17.5 W/mm^2, a LF of 2652.2 lm, a CCT of 2604 K, and a significantly improved CRI of 91.2. The superior optical performance is attributed to the effective protection of phosphor properties enabled by the CSP process, which preserves luminescent efficiency under high-power excitation. At an LPD of 10 W/mm^2, the Y/R-PF@Cu converter exhibits a high thermal conductivity of 50.6 W/(m·K), along with excellent heat dissipation and a peak hotspot temperature of 327℃, resulting from the synergistic thermal management provided by the matrix and Cu substrate. The optimized Y/R-PF@Cu-based white laser source delivers high luminance with vivid, natural color rendering, closely matching daylight conditions. This work proposes a low-temperature PF fabrication strategy for strongly alternative color converters, expanding their application scope and enhancing overall performance.

Author contributions

Jiuzhou Zhao: Conceptualization, Methodology, Writing- Original draff. **Meiqi Ye:** Data curation Visualization. **Wenhao Zhang:** Investigation. **Guankai Wang:** Validation. **Yun Mou:** Writing- Reviewing and Editing. **Yang Peng:** Resources, Supervision.

Acknowledgements

The authors would like to thank the Analytical and Testing Center of Huazhong University of Science and Technology for the support in PL, PLE, SEM, decay measurements.

References

[1] Li S, Wang L, Hirosaki N, et al. Color conversion materials for high-brightness laser-driven solid-state lighting. *Laser Photonics Rev* 2018, 12: 1800173.

[2] Denault KA, Cantore M, Nakamura S, et al. Efficient and stable laser-driven white lighting. *AIP Adv.* 2013, 3: 072107.

[3] Wang P, Lin H, Chen G, et al. Rapid sintering of high-efficiency phosphor-in-glass films for laser-driven light source. *Nat. Commun.* 2025, 16: 2807.

[4] Zheng P, Li S, Wei R, et al. Unique design strategy for laser-driven color converters enabling superhigh-luminance and high-directionality white light. *Laser Photonics Rev.* 2019, 13: 1900147.

[5] Zhao J, Guo Z, Yu Z, et al. Laser-driven white light source with high luminescence saturation through reflective color converter. *IEEE Electron Device Lett.* 2023, 45: 232-235.

[6] Yang Z, Zheng S, Xi G, et al. Patterned phosphor-in-glass films with efficient thermal management for high-power laser projection displays. *J. Adv. Ceram.* 2023, 12: 2075-2086.

[7] Kumar D, Varshney RK, Mehta DS. Enhanced optical performance and thermal stability of screen-printed color-converter composite films for laser-driven-white lighting. *Electron. Mater.* 2025, 7:

11149-11164.

[8] Ma Y, Luo X. Packaging for laser-based white lighting: status and perspectives. *J. Electron. Packag.* 2020, 142: 010801.

[9] Zhang YQ, Liu JM, Zhang YJ, et al. Robust YAG:Ce single crystal for ultra-high efficiency laser lighting. *J. Rare Earths* 2022, 40: 717-724.

[10] Xu L, Wang L, Bao S, et al. High-efficiency yellow-emitting $La_3Si_6N_{11}$:Ce phosphor-in-glass for laser-driven white lighting. *Ceram. Int.* 2022, 48: 23955-23962.

[11] Wang G, Zhu Q, Nie S, et al. Innovative architecture for phosphor-in-glass films enabling superior luminance and color quality laser-driven white light. Laser Photonics Rev. 2024, 18: 2301263.

[12] Y Mou, Y Peng, X Wang, et al. Unique sandwich and microstructure design of phosphor-in-glass film for high brightness laser-driven white lighting. *J. Eur. Ceram. Soc.* 2024,18: 2301263.

[13] Yang Z, Lin S, Zheng S, et al. High-efficiency red-emitting phosphor-in-glass films for laser-driven lighting and display. *Laser Photonics Rev.* 2025, 20: e02185.

[14] Tian R, Zhou T, Xie R, et al. Spectrally tunable dual-phosphor ceramics for laser lighting. *Laser Photonics Rev.* 2025, 19: 2402144.

[15] Wang Y, Huang X, Cheng Z, et al. Al_2O_3–Ce:YAG composite phosphor ceramics for white laser lighting: Novel preparation and regulatable properties. *J. Am. Ceram. Soc.* 2023, 106: 5933-5943.

[16] Du B, Li W, Zhang L, et al. Recent advances in preparing transparent phosphor ceramics for high-index color rendering and high-power lighting. *Molecules* 2024, 29: 1325.

[17] Hu P, Shi Y, Du Q, et al. Ceramic phosphors for laser-driven lighting. *Rev. Mater. Res.* 2025, 1: 100092.

[18] Peng Y, Yu Z, Zhao J, et al. Unique sandwich design of high-efficiency heat-conducting phosphor-in-glass film for high-quality laser-driven white lighting. *J. Adv. Ceram.* 2022, 11: 1889-1900.

[19] Chen X, Liu M, Chen H, et al. High luminous efficiency and excellent thermal performance in

rod-shaped YAG:Ce phosphor ceramics for laser lighting. *Opt. Express* 2024, 32: 1465-1477.

[20] Liu Z, Kang J, Min C, et al. Ceramic-phosphor composite architecture enabling high-power laser-driven warm white lighting with enhanced color fidelity. Opt. Express, 2025, 33: 31482-31495.

[21] Lai Y, Zheng J, Zhang Z, et al. Core-cladding-like phosphor ceramics wafer: A path to ultra-high luminance. *J. Adv. Ceram.* 2025, 14: 9221137.

[22] Kuang Y, Sun Y, Chen W, et al. Integrating high efficiency and thermal reliability photoluminescence in double-sapphire-sandwiched phosphor-in-glass film for laser projection displays. 2026, 36: e20133.

[23] Li S, Guo Y, Xie R. Laser phosphors for next-generation lighting applications. *Acc. Mater. Res.* 2022, 3:1299-1308.

[24] Shen Z, Zhu Q, Tian R, et al. Investigation of excitation modes in Al_2O_3-YAG phosphor ceramics for high-power laser-driven lighting. *ECS J. Solid State Sci. Technol.* 2024, 13: 046002.

[25] Ye W, Li M, Li S, et al. A novel red-emission $Ca_2LaTiAl_3O_{12}$:Eu^{3+} phosphor with garnet structure and high stability for high-CRI white light-emitting devices. *Lumin.* 2025, 281: 121217.

[26] Chen W, Cao D, Dong Y, et al. Enhancing luminous flux and color rendering of laser-excited YAG:Ce^{3+} single crystal phosphor plate via surface roughening and low-temperature sintering a $CaAlSiN_3$:Eu^{2+} phosphor-in-borate glass. *Lumin.* 2022, 251: 119225.

[27] Mou Y, Zhao J, Yu Z, et al. Highly reflective interface design for phosphor-in-glass converter enabling ultrahigh efficiency laser-driven white lighting. *J. Eur. Ceram. Soc.* 2022, 16: 7579-7586.

[28] Hu C, Liu Z, Luo W, et al. Test methods for optical and opto-functional transparent ceramics. *Advanced Ceramics* 2025, 46: 286-326.

[29] Jiang Z, Yuan S, Xu J, et al. High color rendering and high-luminance laser lighting using all inorganic nitride phosphor films. *RSC Adv.* 2023, 13: 25561.

[30] Chen X, Yuan S, Guo Y, et al. Ce^{3+}-based phosphor converter enabling laser lighting to attain both high CRI and high luminous efficacy. *Ceram. Int.* 2023, 49: 40846.

[31] Zhu D, Nikl M, Chewpraditkul W, et al. Development and prospects of garnet ceramic scintillators: A review. *J. Adv. Ceram.* 2022, 11: 1825-1848.

[32] Pang Q, Liu W, Shen J, et al. Improved optical properties of BN powder shielded Ce:YAG ceramics prepared by hot pressing. *Ceram. Int.* 2022, 48: 23821-23827.

[33] Fang H, Li L, Zhou B, et al. Reactive spark plasma sintering of YAG–YAG:Ce composite phosphor ceramics for laser-driven lighting with high luminous efficacy. *J. Mater. Chem.* C 2025, 13: 4781-4790.

[34] Liang Y, Zhang Y, Yang H, et al. The excellent luminous efficiency and high thermal stability of phosphor-in-glass for high-power laser. *Appl. Phys. Lett.* 2021, 119: 033303.

[35] Huang Q, Lin H, Wang B, et al. Patterned glass ceramic design for high-brightness high-color-quality laser-driven lightings. *J. Adv. Ceram.* 2022, 11: 862-873.

[36] Xi G, Lin S, Shen T, et al. Transparent ceramic@sapphire composites for high-power laser-driven lighting. *Adv. Sci.* 2025, 12: 2505232.

[37] Yang Z, Liu Y, Yang X, et al. Large-sized $Y_3Al_5O_{12}$: Ce^{3+}/Al_2O_3 composited ceramics for laser-driven lighting sources. *J. Am. Ceram. Soc.* 2026, 109: e70592.

[38] Yang Z, Wu B, Gao M, et al. Highly stable phosphor in glass-ceramic film composites for laser-driven lighting sources. *Laser Photonics Rev.* 2026, 0: e71407.

[39] Wang G, Xiong W, Qiu L, et al. Second-level fast sintering enables high-brightness light source for visible light communication. *Nat. Commun.* 2026, 17: 7973.

[40] Vojtěch Nečina. Transparent ceramics by cold sintering process – Challenges and opportunities. *J. Eur. Ceram. Soc.* 2025, 45: 117519.

[41] Haribabu P, Pathan S, Sang-Min H, et al. Densification and grain growth in ceramics fabricated by cold sintering: A review on the effect of process parameters. *J. Am. Ceram. Soc.* 2026, 109: e70268.

[42] G Jie, Xia Z, Ding Q, et al. Cold sintering of highly transparent calcium fluoride nanoceramic as a universal platform for high-power lighting. *Adv. Funct. Mater.* 2023, 33: 2302088.

Availability of data and materials

The data that support the findings of this study are available from the corresponding author upon reasonable request.

Competing interests

The authors have no competing interests to declare that are relevant to the content of this article.